Turnkey Automated Design of Handset Antenna Systems for Enhanced Cellular and SATCOM Performance Based on Internal Multiport Method

Wenrui Zheng, *Student Member, IEEE*, Yunlai Yang, *Student Member, IEEE*, Yan Wang, *Senior Member, IEEE*, Can Ding, *Senior Member, IEEE*, and Hui Li, *Senior Member, IEEE*

***Abstract*—Designing multi-antennas with multiple functions covering all the bands in a compact handset platform presents substantial challenges in impedance matching, decoupling, and radiation pattern synthesis, especially under user interaction and integration constraints. This paper proposes a turnkey design framework based on the internal multiport method (IMPM), which leverages scattering matrix formulations to enable matrix-based evaluation of antenna performance without manual analysis or mode identification. By integrating this model into the NSGA-III evolutionary algorithm, the entire antenna configuration is optimized holistically as a package, including feeding port placement, reactive load tuning, and shorting control. Different from conventional designs that focus on a single or limited number of antenna elements, the proposed framework automatically synthesizes a four-antenna cellular system and a dual-antenna satellite system on the same platform. Both states share the same hardware and can be reconfigured using only five switching points. The cellular state supports 2×2 and 4×4 MIMO operation across 0.69 to 4.2 GHz, while the satellite state achieves wide-beam endfire radiation in the n256 band with a 4.6 dB gain improvement. Prototypes were fabricated, and measurements demonstrated close agreement with simulations, validating the effectiveness of the proposed approach.**

***Index Terms*—Handset antenna system, cellular antenna system, satellite communication, impedance matching, pattern synthesis, internal multiport method, NSGA-III, endfire radiation, reconfigurable antenna.**

I. Introduction

THE rapid growth of mobile communication has made smartphones indispensable platforms for services such as voice, data, positioning, and multimedia [1], [2]. As the key RF component enabling signal transmission and reception, the handset antenna system directly determines communication performance [3], [4], and its design has therefore remained a central topic in both academia and industry.

With the growing spectral complexity from GSM to 5G, handset antennas face increasing demands for compactness [5], [6], [7], [8], broadband coverage [9], [10], [11], [12], [13], and isolation [14], [15], [16], [17], [18]. Representative solutions include folded loops with tunable feed–short distances to extend high-band coverage [5], dual-monopole structures with ground branches for broadband operation under metal frames [9], and shared-radiator designs exploiting common–differential mode cancellation for self-decoupling [14].

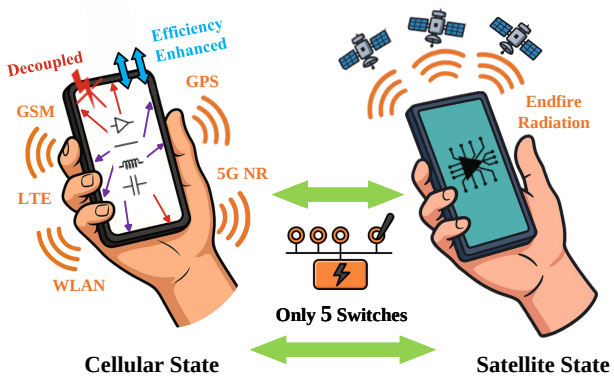

Fig. 1. Illustration of the overall design concept.

In practical scenarios, handset antennas suffer efficiency degradation under user interaction, making high radiation efficiency a critical design target. Traditional solutions include metamaterials [19], zeroth-order resonance (ZOR) structures [20], multi-antenna switching [21], [22], and characteristic mode (CM) theory [23], [24], [25], [26]. In [20], a via-less CRLH ZOR antenna achieves over 30% efficiency on tissue phantoms. In [24], a CMA-based handset antenna applies adaptive excitation through antenna clusters to suppress hand effects, but requires complex multi-channel RF hardware. In [25], CM analysis is used to reveal efficiency degradation in lossy smartphones, where suppressing higher-order modes improves IFA efficiency.

Beyond terrestrial networks, handset antennas are increasingly required to support satellite connectivity through endfire radiation with large beamwidth [27], [28], [29], [30], [31], [32], [33]. Reported solutions include foldable-phone dipole arrays achieving CP at specific deployment angles [28], compact dual-antenna structures with parasitic branches for wide endfire coverage in the n256 band [29], and inverted-L designs with reactive loading to enhance upper-hemisphere performance [33].

Although prior studies have advanced both design method-

This work was supported by: (1) National Natural Science Foundation of China (624B2031; 62371089); (2) Dalian Excellent Young Science and Technology Talents Project (2023RY015). (*Corresponding Author: Hui Li*)

W. Zheng, Y. Yang, and H. Li are with the School of Information and Communication Engineering, Dalian University of Technology, Dalian 116024, China. H. Li is also with the Research Institute of Electrical Communication, Tohoku University, Sendai 980-8577, Japan (e-mail: wr.zheng@mail.dlut.edu.cn; hui.li@dlut.edu.cn).

Y. Wang is with the Key Laboratory for Information Science of Electromagnetic Waves (MoE), School of Information Science and Technology, Fudan University, Shanghai 200433, China.

C. Ding is with the Global Big Data Technologies Center, University of Technology Sydney, Ultimo, NSW 2007, Australia.

ology and antenna performance, assembly level integration remains a central challenge in practical handsets. Specifically, multiple antennas share the metal frame and ground, operate within a tightly coupled volume, while the display and the user hand introduce additional losses and parasitic currents. These interactions can degrade efficiency and impedance stability and often necessitate empirical retuning. Consequently, designs defined at the unit or module level seldom transfer directly to the full device, particularly for frame-integrated handsets. The internal multiport method (IMPM), despite the advantages of a low-dimensional formulation and numerical accuracy, has likewise been applied mainly at the unit or module level rather than at the assembly level. Representative applications include MIMO pixel antennas [34], rectennas for ambient RF energy harvesting [35], multiband pixel antenna [36], single circularly polarized GPS smartwatch antenna [37], polarization-reconfigurable antennas [38], and decoupling of closely spaced patch antennas [39]. Accordingly, these considerations motivate a holistic and algorithmically unified assembly level framework based on IMPM.

In this paper, a turnkey automated framework is proposed for goal-driven synthesis of multi-antenna handset systems. Instead of treating impedance matching, decoupling, efficiency, and radiation pattern synthesis separately, these objectives are cast as a unified optimization problem based on the frequency-dependent scattering matrix. Embedding this network model into an evolutionary algorithm yields directly deployable antenna configurations without empirical tuning. Using this approach, a four-antenna cellular system is realized on a metal-framed handset with high efficiency and low correlation across 0.69–4.2 GHz (GSM, LTE, 5G NR, and 2.4 GHz WLAN). The same hardware is further reconfigured through five optimized switches into a satellite state supporting dual-band positioning and endfire radiation in the n256 band. This state-sharing design provides robust terrestrial and satellite performance under realistic scenarios, as illustrated in Fig. 1.

The contributions of this work are summarized as follows: 1) A unified algorithmic framework based on the internal multiport method is developed, enabling holistic optimization of impedance matching, decoupling, mitigation of hand effects, and radiation pattern control in a single automated process. 2) The framework facilitates the goal-oriented synthesis of a four-antenna cellular MIMO system on a compact metal-framed handset, achieving high radiation efficiencies and good isolations across 0.69–4.2 GHz. 3) Antenna reconfiguration within the complex antenna assembly has also been taken into account. Building upon the optimized cellular MIMO system, one antenna element is reconfigured using only five PIN diodes to support endfire SATCOM radiation under user scenarios.

The remainder of this paper is organized as follows. Section II formulates the design problem as a multi-objective optimization and introduces the proposed framework. Section III demonstrates the automated synthesis of a four-antenna cellular system on a metal-framed handset and its reconfiguration into a satellite state with endfire radiation. Section IV reported experimental validation, and Section V concludes the paper.

II. Problem Formulation

Under the assumption that channel state information is unavailable at the transmitter, the MIMO channel capacity incorporating port efficiency is given by: [40], [41]

$$C = \log_2 \det\Big(\mathbf{U}_{N_R} + \frac{P}{N_T N_0}\,\mathbf{H}\mathbf{H}^{\mathrm{H}}\Big), \tag{1}$$

where $\mathbf{U}_{N_R}$ denotes the $N_R \times N_R$ identity matrix, N_R and N_T are the numbers of receive and transmit antennas, P is the total transmit power, and N_0 the noise spectral density. The channel matrix $\mathbf{H}$ is modeled as:

$$\mathbf{H} = \mathbf{T}^{1/2}\mathbf{R}^{1/2}\mathbf{W}, \tag{2}$$

where $\mathbf{T} = \mathrm{diag}(\eta_1, \ldots, \eta_{N_T})$ denotes the diagonal matrix of port efficiencies, $\mathbf{W} \in \mathbb{C}^{N_R \times N_T}$ is an i.i.d. Rayleigh fading matrix, and $\mathbf{R} \in \mathbb{C}^{N_T \times N_T}$ the spatial correlation matrix determined by far-field directivity patterns. Each element of $\mathbf{R}$ is given by [42]:

$$\mathbf{R}_{pq} = \int_{4\pi} \mathbf{D}_p^*(\Omega)\,\mathbf{D}_q(\Omega)\,\mathrm{d}\Omega, \tag{3}$$

where $\mathbf{D}_p(\Omega)$ denotes the complex pattern of port p, normalized to unit radiated power. Efficiency determines the signal power, while inter-antenna correlation affects the rank of the channel matrix $\mathbf{H}$. Therefore, in practical cellular antenna design, achieving high efficiency and low correlation is essential.

To achieve this, the following subsections derive the port reflection, mutual coupling, radiation efficiency, and far-field patterns of the cellular antenna system using the IMPM with multiple load configurations. The formulation is expressed in terms of scattering parameters, which have been shown to provide good computational efficiency [39]. The system topology, including feeding and loading configurations, is represented by a decision vector $\mathbf{x}$ that is optimized automatically through an evolutionary algorithm.

A. Encoding Structure of the Decision Vector

In the automated design procedure, N_p denotes the total number of discrete ports in the handset antenna network, including both external and internal ones. Among them, N_f external ports are used for excitation, and N_l internal ports are reserved for reactive loading. The decision vector consists of continuous variables within $[-1, 1]$, which ensures consistency and improves optimization efficiency:

$$\mathbf{x} = [x_1,\ x_2,\ x_3,\ x_4]^T \in \mathbb{R}^{N_d}. \tag{4}$$

Each segment of the decision vector serves a specific role. The subvector $x_1 \in \mathbb{R}^{N_p}$ encodes the open or short states of all discrete ports, and the port-termination vector $\boldsymbol{\delta}$ is obtained by thresholding x_1:

$$\boldsymbol{\delta} = [\,\delta_1, \ldots, \delta_{N_p}\,]^T, \tag{5}$$

$$\delta_i = \begin{cases} 1, & x_{1,i} > 0, \\ 0, & x_{1,i} \le 0, \end{cases} \quad i = 1, \ldots, N_p. \tag{6}$$

Herein, $\delta_i = 1$ indicates a short-circuited port, while $\delta_i = 0$ corresponds to an open port.

TABLE I
AVAILABLE VALUES FOR REACTIVE COMPONENTS

Capacitors (pF)										
0.5	0.6	0.7	0.8	0.9	1.0	1.1	1.2	1.3	1.4	1.5
1.6	1.7	1.8	1.9	2.0	2.2	2.4	2.7	3.0	3.3	3.6
3.9	4.3	4.7	5.1	5.6	6.2	6.8	7.5	8.2	9.1	10
12	15	18	22	27	33	39	47	68		
Inductors (nH)										
0.6	0.7	0.8	0.9	1.0	1.1	1.2	1.3	1.4	1.5	1.6
1.7	1.8	1.9	2.0	2.1	2.2	2.3	2.4	2.7	2.9	3.0
3.3	3.4	3.6	3.9	4.3	4.7	5.1	5.6	6.2	6.8	7.5
8.2	9.1	10	11	12	15	18	33			

The subvectors $x_2 \in \mathbb{R}^{N_f}$ and $x_3 \in \mathbb{R}^{N_l}$ are linearly mapped and rounded to integer indices from 1 to N_p, then processed by a conflict-avoidance mechanism to generate two disjoint index sets $\mathcal{E} \subset \{1, \ldots, N_p\}$ and $\mathcal{L} \subset \{1, \ldots, N_p\} \setminus \mathcal{E}$, with $\mathcal{E} \cap \mathcal{L} = \emptyset$, representing the feeding and loading ports. The subvector $x_4 \in \mathbb{R}^{N_l}$ prescribes the reactive loads on $\mathcal{L}$, where the sign of each entry specifies a capacitor C_i or inductor L_i, and the magnitude indexes into the component libraries $\{C_1, \ldots, C_{N_C}\}$ and $\{L_1, \ldots, L_{N_L}\}$ listed in Table I. Hence, the total dimension of the decision vector is:

$$N_d = N_p + N_f + 2N_l. \tag{7}$$

B. Antenna Performance Metrics Calculation Based on Scattering Matrices

The scattering network parameters vary with frequency. For frequency-specific evaluations, two frequency sets are defined:

$$\mathcal{F}_m = \{f_1, \ldots, f_{N_m}\}, \quad \mathcal{F}_e = \{\tilde{f}_1, \ldots, \tilde{f}_{N_e}\} \subseteq \mathcal{F}_m, \tag{8}$$

where scattering-related metrics are computed for $f \in \mathcal{F}_m$, whereas current vectors, far-field patterns, and radiation efficiencies are evaluated for $f \in \mathcal{F}_e$. As shown in (8), the evaluation set $\mathcal{F}_e$ is a subset of $\mathcal{F}_m$, since radiation-related quantities are more computationally expensive and thus need not be sampled as densely.

At each frequency $f \in \mathcal{F}_m$, the impedance seen at a loaded internal port $i \in \mathcal{L}$ is given by:

$$Z_i(f) = \begin{cases} \dfrac{1}{j\,2\pi f\,C_i}, & \text{for capacitive loading,} \\ j\,2\pi f\,L_i, & \text{for inductive loading,} \end{cases} \tag{9}$$

while for $i \notin \mathcal{L}$ the port is treated as an ideal termination given by its discrete topology: short-circuited if $\delta_i = 1$ and open-circuited if $\delta_i = 0$. With Z_0 denoting the reference impedance, the reflection coefficient at each internal port $i \notin \mathcal{E}$ is given by:

$$\Gamma_i(f) = \frac{Z_i(f) - Z_0}{Z_i(f) + Z_0}, \quad f \in \mathcal{F}_m, \tag{10}$$

which form the diagonal entries of the reflection coefficient matrix $\mathbf{\Gamma}_{\text{int}}(f) \in \mathbb{C}^{N_i \times N_i}$, with $N_i = |\{1, \ldots, N_p\} \setminus \mathcal{E}|$.

The full scattering matrix $\mathbf{S}(f)$ of the antenna network at frequency $f \in \mathcal{F}_m$ is denoted and partitioned according to the feed ports $\mathcal{E}$ and the internal ports $\{1, \ldots, N_p\} \setminus \mathcal{E}$, resulting in:

$$\mathbf{S}(f) = \begin{bmatrix} S_{FF}(f) & S_{FI}(f) \\ S_{IF}(f) & S_{II}(f) \end{bmatrix}, \tag{11}$$

where the off-diagonal submatrices represent interactions between feed (F) and internal (I) ports. Accounting for internal-port terminations through the reflection matrix $\mathbf{\Gamma}_{\text{int}}(f)$, the equivalent scattering matrix at the feeding ports is given by:

$$\mathbf{S}_{\text{eq}}(f) = S_{FF}(f) \; + \; S_{FI}(f) \left(\mathbf{\Gamma}_{\text{int}}(f) - S_{II}(f)\right)^{-1} S_{IF}(f). \tag{12}$$

The total port current vector $\mathbf{I}_{\text{tot}}(f) \in \mathbb{C}^{N_P}$ is evaluated at each $f \in \mathcal{F}_e$ by exciting a feed port $k \in \mathcal{E}$ with normalized incident power P_0. For each excitation, the forward-traveling voltage vector $\mathbf{V}^+(f) \in \mathbb{C}^{N_P}$ is defined as:

$$\mathbf{V}^+(f) = \begin{bmatrix} \mathbf{V}_F^+(f) \\ \mathbf{V}_I^+(f) \end{bmatrix}, \tag{13}$$

where $\mathbf{V}_F^+(f) \in \mathbb{R}^{N_f}$ has a single nonzero entry $\sqrt{P_0}$ at the k-th feed port and zeros elsewhere. The internal-port forward wave $\mathbf{V}_I^+(f) \in \mathbb{C}^{N_i}$ is then obtained as:

$$\mathbf{V}_I^+(f) = \left(\mathbf{\Gamma}_{\text{int}}(f) - S_{II}(f)\right)^{-1} S_{IF}(f)\, \mathbf{V}_F^+(f), \tag{14}$$

which accounts for wave propagation into the terminated internal ports. The total currents at all ports are obtained from the incident and reflected waves via:

$$\mathbf{I}_{\text{tot}}(f) = \frac{1}{Z_0}\Big(\mathbf{V}^+(f) \; - \; \mathbf{S}(f)\, \mathbf{V}^+(f)\Big), \tag{15}$$

where Z_0 is the reference impedance. The current vector $\mathbf{I}_{\text{tot}}(f)$ contains the excitation-induced responses across all ports of the network.

Following current synthesis, the far-field radiation is evaluated at each $f \in \mathcal{F}_e$. The θ- and φ-components of the single-port responses are stored in $\mathbf{E}_\theta^{\text{sp}}(f), \mathbf{E}_\varphi^{\text{sp}}(f) \in \mathbb{C}^{N_{\text{dir}} \times N_P}$, where columns correspond to excited ports and rows to sampled directions. With uniform angular sampling at 10° in both elevation and azimuth, the total number of directions is $N_{\text{dir}} = 684$.

The synthesized far-field vectors $\mathbf{E}_\theta(f), \mathbf{E}_\varphi(f) \in \mathbb{C}^{N_{\text{dir}}}$ are obtained through matrix–vector multiplication:

$$\mathbf{E}_\theta(f) = \mathbf{E}_\theta^{\text{sp}}(f)\, \mathbf{I}_{\text{tot}}(f), \tag{16}$$

$$\mathbf{E}_\varphi(f) = \mathbf{E}_\varphi^{\text{sp}}(f)\, \mathbf{I}_{\text{tot}}(f). \tag{17}$$

The power density vector $\mathbf{S}(f) \in \mathbb{R}^{N_{\text{dir}}}$ is then computed element-wise as:

$$\mathbf{S}(f) = \frac{|\mathbf{E}_\theta(f)|^2 + \left|\mathbf{E}_\varphi(f)\right|^2}{2\,\eta_0}, \tag{18}$$

where $\eta_0 = 377\,\Omega$ is the free-space wave impedance. Subsequently, the total radiated power $P_{\text{rad}}(f)$ is obtained by numerical integration over all sampled directions:

$$P_{\text{rad}}(f) = \sum_{n=1}^{N_{\text{dir}}} \mathbf{S}_n(f) \; \sin\theta_n \, \Delta\theta \, \Delta\varphi. \tag{19}$$

The radiation efficiency $\eta(f)$ is evaluated as the ratio of radiated power to total input power:

$$\eta(f) = \frac{P_{\text{rad}}(f)}{\mathbf{I}_{\text{tot}}^*(f)\, \mathbf{R}(f)\, \mathbf{I}_{\text{tot}}(f)}, \tag{20}$$

where $\mathbf{R}(f) = \Re\{\mathbf{Z}(f)\}$ is the real part of the port impedance matrix. The impedance matrix $\mathbf{Z}(f)$ is obtained from the scattering matrix as:

$$\mathbf{Z}(f) = Z_0 \left(\mathbf{U} + \mathbf{S}(f)\right) \left(\mathbf{U} - \mathbf{S}(f)\right)^{-1}, \tag{21}$$

where $\mathbf{U} \in \mathbb{R}^{N_P \times N_P}$ is the identity matrix.

The realized gain pattern in decibels is computed based on the power flow density. Specifically, the realized gain vector $\mathbf{G}_{\text{realized}}(f) \in \mathbb{R}^{N_{\text{dir}}}$ at frequency $f \in \mathcal{F}_e$ is given by:

$$\mathbf{G}_{\text{realized}}(f) = 10 \log_{10} \left[\frac{\mathbf{S}(f)}{\mathbf{S}_0} \right], \tag{22}$$

where $\mathbf{S}(f)$ represents the power flow density at frequency f, and $\mathbf{S}_0$ is a reference power density. This formulation accounts for the angular power distribution of the antenna.

In summary, the procedure evaluates frequency-dependent internal port terminations, equivalent scattering matrices, and total current vectors over $\mathcal{F}_m$ and $\mathcal{F}_e$. From these, far-field patterns, radiated power, radiation efficiency, and realized gain are obtained at selected frequencies in $\mathcal{F}_e$.

C. Multi-Objective Functions for Enhanced MIMO Performance

For each feeding port $k = 1, \ldots, N_f$, a set of target frequency subbands is specified as:

$$\mathcal{B}_k = \bigcup_{j=1}^{N_k} \left[f_{k,j}^{\min},\ f_{k,j}^{\max} \right], \tag{23}$$

where each subband $[f_{k,j}^{\min}, f_{k,j}^{\max}]$ specifies the operating range of feeding port k, and N_k is the total number of subbands. Thresholds for matching, coupling, and efficiency are denoted by τ_{match}, τ_{couple}, and τ_η, respectively, and a penalty exponent p controls the severity of threshold violations.

The self-reflection penalty for port k is evaluated over the intersection $\mathcal{B}_k \cap F_m$ as:

$$r_k = \frac{1}{\left|\mathcal{B}_k \cap F_m\right|} \sum_{f_n \in \mathcal{B}_k \cap F_m} \left[\frac{\max\left(0,\ |\mathbf{S}_{\text{eq},kk}(f_n)| - \tau_{\text{match}}\right)}{1 - \tau_{\text{match}}} \right]^p. \tag{24}$$

The mutual-coupling penalty between ports i and j is evaluated over $(\mathcal{B}_i \cup \mathcal{B}_j) \cap F_m$, i.e., the union of their target subbands intersected with the matching set. In this domain, mutual coupling is characterized by $|\mathbf{S}_{\text{eq},ij}|$, and the penalty is defined as:

$$c_{ij} = \frac{1}{\left|(\mathcal{B}_i \cup \mathcal{B}_j) \cap F_m\right|} \sum_{f_n \in \left(\mathcal{B}_i \cup \mathcal{B}_j\right) \cap F_m} \left[\frac{\max\left(0,\ |\mathbf{S}_{\text{eq},ij}(f_n)| - \tau_{\text{couple}}\right)}{1 - \tau_{\text{couple}}} \right]^p. \tag{25}$$

The efficiency penalty for port k is given by:

$$e_k = \frac{1}{\left|\mathcal{B}_k \cap F_e\right|} \sum_{f_n \in \mathcal{B}_k \cap F_e} \left[\frac{\max\left(0,\ \tau_\eta - \eta(f_n)\right)}{\tau_\eta} \right]^p. \tag{26}$$

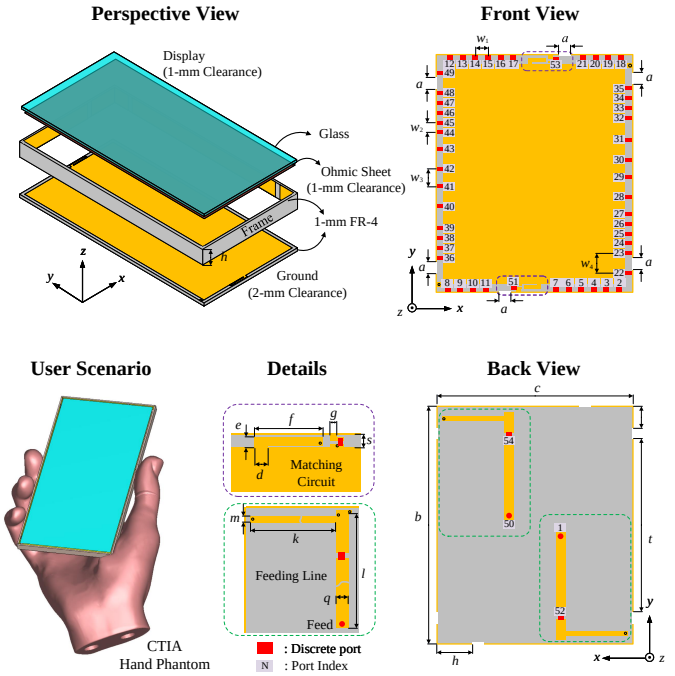

Fig. 2. Physical layout and configuration of discrete ports of the handset platform. Dimensions: $a = 2$ mm, $b = 149$ mm, $c = 75.5$ mm, $d = 2$ mm, $e = 1.6$ mm, $f = 10$ mm, $g = 1$ mm, $h = 20.5$ mm, $k = 22.7$ mm, $l = 70$ mm, $m = 1$ mm, $q = 2$ mm, $s = 6.75$ mm, $t = 131.5$ mm, $w_1 = 6$ mm, $w_2 = 7$ mm, $w_3 = 15$ mm, $w_4 = 9.5$ mm.

Based on the three penalty terms defined above, the objective vector to be minimized is constructed as:

$$\mathbf{f}_{\text{Cell}} = \begin{bmatrix} \dfrac{1}{N_f} \displaystyle\sum_{k=1}^{N_f} r_k \\ \dfrac{2}{N_f(N_f-1)} \displaystyle\sum_{1 \le i < j \le N_f} c_{ij} \\ \dfrac{1}{N_f} \displaystyle\sum_{k=1}^{N_f} e_k \end{bmatrix}. \tag{27}$$

The first component measures the average penalty from self-reflection across all feed ports, quantifying impedance mismatch within each target subband. The second accounts for mutual coupling between port pairs, covering both co-band and cross-band interactions over the union of their subbands. The third quantifies the average efficiency deficit over the far-field evaluation frequencies. The multi-objective optimization problem formulated above will be solved using NSGA-III [43].

D. Multi-Objective Functions for Enhanced Positioning and Standalone SATCOM Capability

In the absence of ground station coverage, satellite communication is essential, requiring sky-directional radiation for stable links. With reference to the coordinate system in Fig. 2, the set of sample indices within the satellite coverage sector is

$$\mathcal{M}_{\text{sat}} = \{\, n : 50^\circ \le \theta_n \le 130^\circ,\ 50^\circ \le \varphi_n \le 130^\circ \}. \tag{28}$$

At the same time, the antenna system should support the GPS L1 and L5 bands for precise dual-frequency positioning. With the self-reflection penalties r_k and mutual-coupling penalties

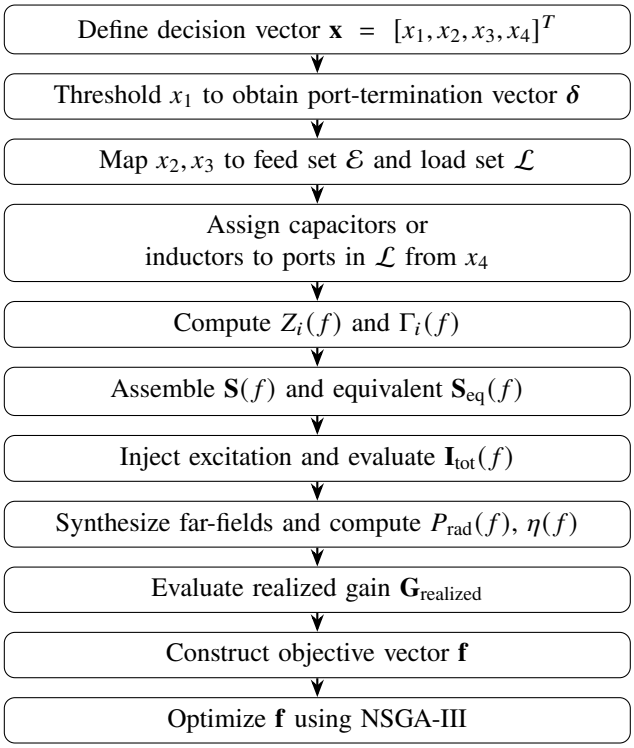

Fig. 3. Automated design workflow of the handset antenna system using the internal multiport method.

c_{ij} defined in (24) and (25), the final three-component objective vector is given by:

$$\mathbf{f}_{\text{SAT}} = \begin{bmatrix} \dfrac{1}{N_f + \frac{1}{2}N_f(N_f-1)} \left(\displaystyle\sum_{k=1}^{N_f} r_k + \sum_{1 \le i < j \le N_f} c_{ij} \right) \\ -\dfrac{1}{|\mathcal{M}_{\text{sat}}|} \displaystyle\sum_{m \in \mathcal{M}_{\text{sat}}} \mathbf{G}_{\text{realized, SAT}}(\theta, \varphi) \\ N_{\text{switch}} \end{bmatrix}. \quad (29)$$

The objective vector $\mathbf{f}_{\text{SAT}}$ in (29) jointly accounts for impedance behavior, radiation performance, and switching complexity in the satellite state. The first term averages the self-reflection penalties r_k and mutual-coupling penalties c_{ij} to penalize mismatches and coupling. The second term evaluates the realized radiation gain within the satellite coverage sector $\mathcal{M}_{\text{sat}}$, computed as the average $\mathbf{G}_{\text{realized, SAT}}(\theta, \varphi)$ over this region. The third term N_{switch} reflects implementation cost by counting the required switches. This formulation promotes impedance matching and directional radiation while limiting reconfiguration overhead. The complete workflow is illustrated in Fig. 3. By integrating impedance, far-field behavior, and hardware constraints into the design vector, the framework establishes a comprehensive basis for goal-oriented assembly-level handset antenna design.

III. Automated Synthesis of Handset Antennas

In this section, the methodology proposed in Section II is applied to a handset model under realistic handheld scenarios, where the entire device is enclosed by the hand phantom according to the CTIA standard [47]. First, the multi-band four-antenna cellular state is synthesized to support conventional usage scenarios, achieving enhanced isolation and radiation efficiency. Then, based on the configuration obtained in the cellular state, a minimal number of 5 switching points is used to efficiently reconfigure the system into satellite state, enabling end-fire radiation at satellite communication bands.

A. Handset Platform Configuration

In modern smartphones, the metallic frame and ground plane serve as the primary radiators. However, their radiation performance is often degraded by the presence of the display and lossy human tissues. Based on this, the handset platform is configured as shown in Fig. 2.

The metallic frame and PCB of the handset are modeled as copper layers printed on a 1-mm-thick FR-4 substrate. The conductivity of the copper is 5.96×10^7 S/m, while the FR-4 material has a relative permittivity of 4.3 and a loss tangent of 0.025. A 2-mm clearance is reserved between the metallic frame and the ground plane, following state-of-the-art handset designs. To emulate the display, a composite layer is introduced, consisting of a 0.5-mm-thick glass and a 0.1-mm-thick ohmic sheet with a surface impedance of 4.5 Ω/sq, separated by a 1-mm clearance from the metallic frame. This ohmic-sheet material, provided by OPPO Inc., serves as a substitute for conventional OLED displays. The glass is characterized by a relative permittivity of 6 and a loss tangent of 0.01. Furthermore, this study employs the CTIA standard hand phantom with frequency-dependent dispersive properties and applies the data-mode handheld configuration specified by the same standard in both full-wave simulations and measurements [47], which has been widely adopted in handset antenna studies [24], [48]. This industry-standard phantom represents an averaged grip across typical hand sizes and postures. Since the phantom is included in all models, the retrieved multiport data inherently characterize the hand-induced loss and coupling, thereby allowing the optimizer to account for these effects without introducing extra parameters. If alternative hand postures are required, the proposed framework can re-extract the corresponding multiport data for re-optimization or jointly optimize across multiple handheld setups to obtain a balanced design.

Six 2-mm-wide discontinuities are introduced along the metal frame to prevent low-efficiency slot-mode excitation between the ground plane and the frame [9], [24]. Within this frame-integrated handset assembly, the metal frame together with the device ground serves as the primary radiator. Although power is fed through localized branches, currents also flow on parasitic frame segments and adjacent conductors, contributing to the overall radiation. As a result, each antenna element behaves as a frame-integrated radiator rather than an isolated branch.

In this work, the IMPM is employed to automate the placement and decoupling design of multiple antennas, with reactive loads implemented as the practical tuning elements. A total of 48 discrete ports (indexed 2–49) are distributed across the clearance regions of the handset platform, serving as candidate locations for excitation or passive loading to enable fine-grained current control. Two additional ports (ports 1 and 50) are reserved as excitations for the two primary antennas. Furthermore, four ports (ports 51–54) are positioned along the

TABLE II
FREQUENCY ALLOCATION $\mathcal{B}_j$ OF EACH ANTENNA PORT IN CELLULAR AND SATELLITE STATES

State	Feeding Port	Allocated Bands (GHz)
Cellular	A	0.7–0.95, 1.7–2.4, 2.4–2.7, 3.3–4.2
	B	0.7–0.95, 1.5–2.4, 2.4–2.7, 3.3–4.2
	C, D	2.4–2.7, 3.3–4.2
Satellite	A, D	Passive
	B	1.55–1.6, 1.98–2.2
	C	1.15–1.2

microstrip lines to facilitate impedance matching. The spatial arrangement of all discrete ports, along with the structural dimensions of the handset platform, is depicted in Fig. 2.

The multiport scattering matrix and the single-port far-field responses are obtained through full-wave simulations, and the impedance matrix for efficiency evaluation is retrieved by (21). Specifically, CST Microwave Studio [49] with the time-domain solver is used over 0–5 GHz, with far-field monitors placed every 0.1 GHz. The display layer and the CTIA-standard hand phantom are consistently included in all simulations. The scattering matrix is retrieved from S-parameter-port excitations under "1D Results", while the embedded radiation patterns are obtained by exciting one current-port with others passive, stored under "Farfields Results". As a result, the scattering/impedance matrix characterizes the network behavior, while the single-port far-field responses describe the radiation characteristics. The final implementation of all discrete ports is optimized within the unified design framework described in Section II.

B. Four-Antenna Cellular State

A four-antenna system operating in cellular state is synthesized based on the methodology proposed in Section II. The target frequency subbands $\mathcal{B}_j$ assigned to the four antennas (Ports A–D) are listed in Table II, covering mainstream communication bands. Specifically, 2×2 MIMO operation is supported over 0.7–0.95 GHz and 1.7–2.4 GHz, while 4×4 MIMO operation is realized over 2.4–2.7 GHz and 3.3–4.2 GHz. In addition, the GPS L1 band is integrated into Port B to enable conventional positioning and navigation functionality.

The frequency sets $\mathcal{F}_m$ and $\mathcal{F}_e$, defined as the union of all subbands $\mathcal{B}_j$ listed in Table II, are used to evaluate impedance matching and radiation efficiency, respectively. The frequency resolution is set to 0.025 GHz for $\mathcal{F}_m$ and 0.1 GHz for $\mathcal{F}_e$. A total of 54 discrete ports are defined on the handset platform. Accordingly, the number of discrete ports is set to $N_p = 54$, and the number of feeding ports is set to $N_f = 4$, corresponding to Ports A–D. The number of loading ports is set to $N_l = 14$, including the matching components assigned to Ports 51–54. Based on this configuration, the total number of decision variables is calculated as $N_d = 86$.

Regarding the port positions, changing the discrete port layout alters both the multiport scattering matrices and the embedded radiation patterns. Nevertheless, in this platform (Fig. 2), the discrete port layout is intentionally dense, with adjacent ports separated by only 6–15 mm, corresponding to about 0.2–0.5 λ_0 at the highest frequency considered in the sub-6 GHz band, where λ_0 denotes the free-space wavelength. Such dense discretization already provides sufficient flexibility for tuning, so

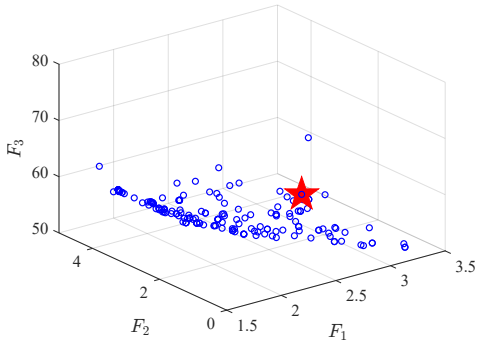

Fig. 4. Three-dimensional Pareto front illustrating the trade-offs among impedance matching, mutual coupling, and radiation efficiencies in the cellular antenna system.

that variations in port locations do not substantially change the optimization degrees of freedom since the overall discretization level remains effectively unchanged. Hence, the optimized performance of the antenna system would not be affected by the port positions as long as the number of ports is sufficient. In practice, the shifts in port positions can be compensated by variations in the reactive load values during optimization, while the problem formulation and the optimization procedure remain unchanged.

The optimization is performed using the NSGA-III algorithm, which is widely adopted for high-dimensional multi-objective electromagnetic problems due to its robustness and diversity-preserving reference-point strategy [43]. Compared with conventional algorithms such as GA or NSGA-II, NSGA-III provides more stable convergence and better coverage of the Pareto front in complex design spaces [44]. The algorithm parameters are set as follows: population size of 300, number of generations of 1000, crossover probability of 1.0, and mutation probability of 0.03. These values follow commonly used settings in related electromagnetic optimization literature [44], [45], [46] and provide a good balance between exploration and convergence efficiency. In general, a smaller population size or fewer generations may cause premature convergence and sub-optimal results, whereas larger values increase computational cost without significant performance gain. The crossover and mutation probabilities regulate the trade-off between solution diversity and convergence stability, where excessively low values cause stagnation and excessively high values introduce unnecessary randomness.

In addition, the thresholds $\tau_{\text{match}}, \tau_{\text{couple}}, \tau_\eta$ are introduced to normalize the objectives and to prevent over-optimization of any single metric, set to 0.4, 0.3, and 0.25, respectively. They correspond to industry-standard values, with $\tau_{\text{match}} = 0.4$ (about −8 dB, within the typical −6 to −10 dB acceptance range), $\tau_{\text{couple}} = 0.3$ (about −10 dB isolation), and $\tau_\eta = 0.25$ (25% efficiency under hand and display loading). Loosening a threshold relaxes its requirement and shifts the Pareto front toward other metrics, whereas tightening it enforces stricter demands and reduces feasible designs. The penalty exponent is set to $p = 3$ to penalize violations strongly but smoothly, avoiding both weak enforcement at small values and unstable convergence at large values, thus preserving reliable convergence with a diverse Pareto set.

TABLE III
MULTIPORT TOPOLOGY CONFIGURATIONS UNDER CELLULAR AND SATELLITE STATES

Ports 1–18																		
Port Index	1	2	3	4	5	6	7	8	9	10	11	12	13	14	15	16	17	18
Cellular	Feed	18.0 nH	Open	Open	Open	Open	Open	Open	Open	Open	Open	Open	Open	Open	Shorted	5.6 pF	Open	Open
Satellite						Shorted		Shorted	Shorted						Open	3.6 pF	Shorted	
Ports 19–36																		
Port Index	19	20	21	22	23	24	25	26	27	28	29	30	31	32	33	34	35	36
Cellular	Open	Open	Open	Open	Shorted	Open	Shorted	Open	Shorted	Shorted	Open	Shorted	7.5 nH	Feed	Open	6.2 nH	5.6 pF	3.9 nH
Satellite							Open	Shorted							Shorted			6.8 nH
Ports 37–54																		
Port Index	37	38	39	40	41	42	43	44	45	46	47	48	49	50	51	52	53	54
Cellular	Open	Shorted	Open	Shorted	4.7 pF	Shorted	Open	3.9 pF	Open	3.4 nH	Shorted	6.2 pF	Feed	Feed	5.1 nH	15.0 pF	5.1 nH	6.2 pF
Satellite				Open		Open			Shorted		Open	33.0 nH						

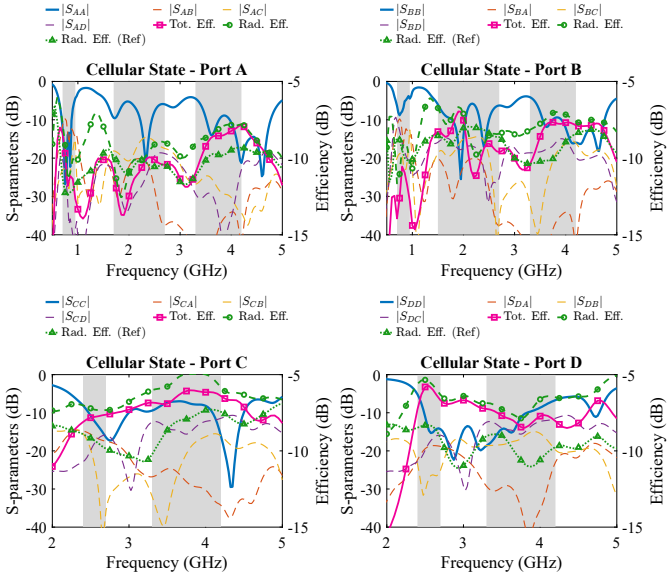

Fig. 5. Simulated *S*-parameters and efficiencies of the proposed handset antennas in cellular state.

With the objective function defined in (27), the algorithm converges in about 2 hours. The resulting Pareto front, shown in Fig. 4, illustrates the trade-offs among impedance matching, coupling, and efficiency, from which a balanced solution marked by a red pentagram is selected and detailed in Table III. Full-wave simulations are conducted in CST Microwave Studio (MWS) to validate the performance of the proposed four-antenna configuration. All reported results are obtained under user interaction conditions, with a hand phantom included in the simulation environment.

The reflection coefficients, transmission coefficients, radiation efficiencies, and total efficiencies of Ports A–D in cellular state are presented in Fig. 5. The corresponding target frequency subbands for each port, as defined in Table II, are highlighted using gray shaded regions. All antennas achieve impedance matching within their target bands, satisfying the −6 dB criterion. Impedance matching in the proposed design is physically realized through the joint tuning of shorting strips and passive reactive loads within the clearance. Their interaction modifies the current paths, the effective electrical length, and thus the input impedance of the specific antenna element. This tuning process is implemented within the internal multiport framework, which characterizes the entire structure as a scattering-matrix-based network and enables the unified tuning of feeding ports, shorting points, and reactive loads. Each element behaves as a platform-integrated radiator rather than an isolated monopole. The worst isolation levels are around 10 dB, demonstrating effective decoupling performance across the entire operating range.

Due to the presence of the lossy display and human tissue, antenna efficiency is inherently limited in practical scenarios. In this study, the radiation efficiencies of the four main antennas without any reactive loads or shorting elements are used as references. These reference configurations exhibit generally lower efficiencies, with noticeable drops observed within certain target bands. With the proposed optimization, the radiation efficiencies of all four antennas are significantly improved under realistic conditions. Owing to the enhanced impedance matching, the total efficiencies are also well preserved.

The radiation patterns of the antennas in the cellular state at representative frequencies (0.8, 2.1, 2.4, and 3.8 GHz) are shown in Fig. 6 as 3D radiation patterns, with the main radiation direction explicitly annotated in each subplot. The corresponding realized gains and total efficiencies are also annotated, further demonstrating the practical viability of the proposed antenna system.

C. Two-Antenna Satellite State

With the advancement of satellite communications, terminal devices are evolving from ground-only connectivity toward standalone satellite capability, introducing three key design challenges. First, metallic frames limit the realization of circular polarization toward sky direction, which is typically required for satellite links. Additionally, a wide-beam endfire radiation pattern is necessary to ensure adequate upward coverage [29]. Second, the presence of nearby antennas and human tissue can significantly distort the radiation pattern, making it difficult to sustain the desired endfire characteristics. Third, state transitions between the cellular and satellite states require switches, and minimizing the number of switching points is critical for practical system integration. These challenges highlight the importance of addressing endfire antenna design at the assembly level rather than the unit/module level, taking into account the full constraints of the device environment.

To address the challenges outlined above, the proposed network-based method incorporates practical endfire satellite communication capability on top of the existing cellular-state antenna, enabling seamless platform integration and efficient

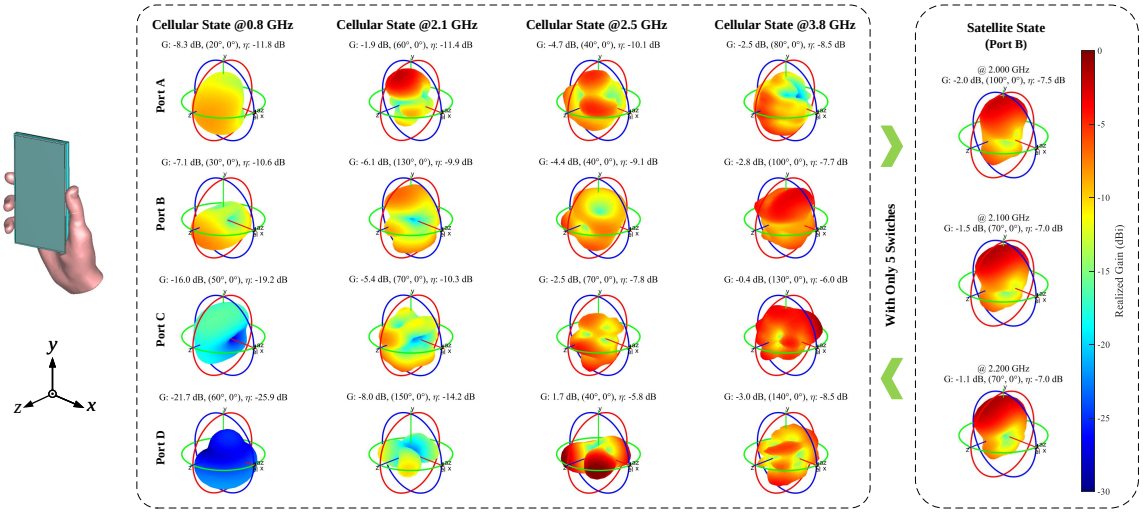

Fig. 6. Simulated 3D radiation patterns of the antenna assembly under cellular and satellite operating states, with realized gains, main radiation direction, and total efficiencies annotated in each subplot. Here, G denotes the maximum realized gain, the pair (θ, φ) indicates the direction of maximum radiation, and η denotes the total efficiency.

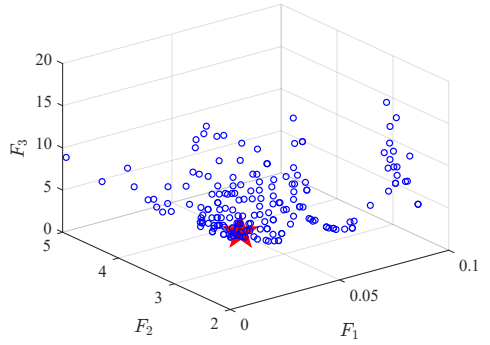

Fig. 7. Three-dimensional Pareto front for satellite state optimization, illustrating the trade-offs among S-parameters, endfire directivity, and implementation complexity.

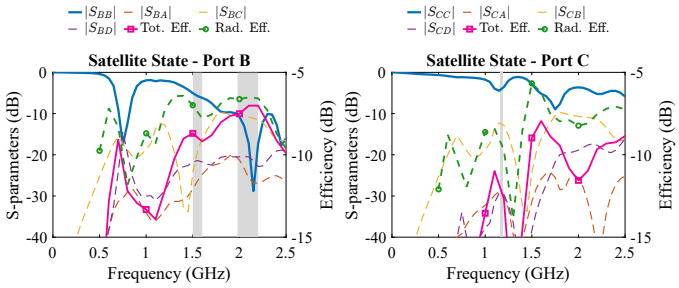

Fig. 8. Simulated S-parameters and efficiencies of the proposed handset antennas in satellite state.

state switching. Building on the cellular-state configuration, Ports B and C are reused as the feeding ports in satellite mode, while the Ports A and D are passively terminated. The supported satellite frequency bands are summarized in Table II, including the GPS L1 band (1.55–1.60 GHz), the GPS L5 band (1.15–1.20 GHz), and the n256 band (1.90–2.20 GHz), which are specified by 3GPP as a standard satellite communication band for mobile terminals [51]. Accordingly, the antenna system in the satellite mode is configured to operate across these three bands, supporting accurate dual-band GPS positioning and wide-beam endfire radiation for satellite communication.

According to the objective function defined in (29), the optimization is performed using the NSGA-III algorithm with a population size of 300. The threshold parameters τ_{match}, τ_{couple}, and τ_{η} are set to 0.4, 0.3, and 0.25, respectively, to prevent over-optimization of individual objectives. The penalty exponent is set to $p = 3$ to impose stronger penalties on constraint violations. The algorithm converges in approximately 40 minutes, with the resulting Pareto front shown in Fig. 7, revealing the trade-offs among S-parameters, endfire directivity, and implementation complexity.

To prioritize low-complexity solutions, configurations requiring only five switching points are first selected. Among these candidates, the solution achieving an average gain of -2.5 dBi is further chosen. The selected point is marked with a red pentagram in Fig. 7, and the corresponding topology configuration is detailed in Table III. It is worth noting that a state flip from shorted to open or vice versa is counted as a single switching operation, since both directions represent the same type of reconfiguration. Compared with the cellular state, switching to the satellite state requires only five switch operations, two of which involve simple state flips between open and short. The remaining three switches, located at Ports 16, 36, and 48, are used for loading reconfiguration. This efficient transition from cellular to satellite state demonstrates the practicality of the proposed configuration reuse strategy.

The simulated S-parameters and efficiencies of Ports B and C in the satellite state are presented in Fig. 8. Good impedance matching is achieved across all three target frequency bands. In terms of efficiency, taking the performance of Port B in the cellular state (see Fig. 5) as a reference, the radiation efficiency within the n256 band is further improved in the satellite state, remaining above -7 dB across the entire band. At 2.1 GHz, the efficiency is 2.9 dB higher than that of the same antenna in the cellular state. These results clearly demonstrate the flexibility and effectiveness of the proposed efficiency enhancement strategy.

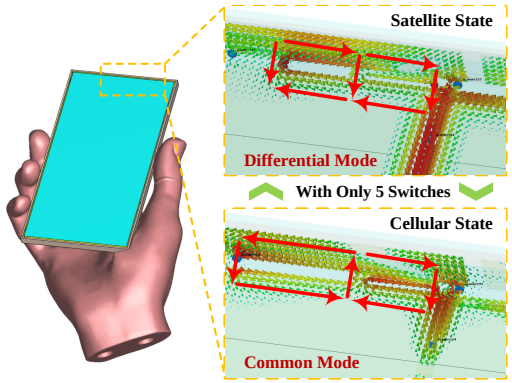

Fig. 9. Simulated surface current distributions of the antenna system in the (a) cellular state and (b) satellite state.

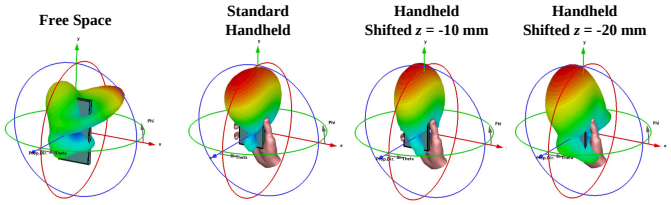

Fig. 10. Radiation patterns of the SATCOM antenna (Port B) at 2.1 GHz under different scenarios (linear scale), including free space, standard hand phantom, and the phantom shifted by 10 mm and 20 mm toward the back cover.

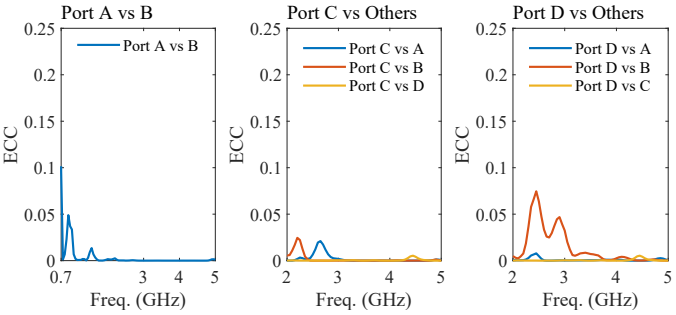

Fig. 11. Simulated envelope correlation coefficients (ECCs) under individual port excitations in the cellular state.

The radiation patterns of the antenna system in the satellite state at 2.0 GHz, 2.1 GHz, and 2.2 GHz are illustrated in Fig. 6. Using the 2.1 GHz pattern of Port B in the cellular state (near the n256 band) as a reference, it is observed that Port B in the satellite state achieves a clearly endfire-directed radiation pattern within the n256 band. In contrast, the reference pattern exhibits dispersed radiation over a wide range of solid angles, with a realized gain of −6.1 dBi, which is significantly lower than the −1.5 dBi gain achieved by the reconfigured satellite antenna.

The current distributions of the antenna system in the cellular and satellite states are illustrated in Fig. 9. It can be observed that the antennas exhibit distinct common-mode and differential-mode current distributions in the cellular and satellite states, respectively, consistent with the characteristics reported in [14]. Such differential-mode excitation in the satellite state contributes to the formation of endfire radiation.

To further evaluate robustness against grip variations, the CTIA hand phantom is shifted by 10 mm and 20 mm toward the back cover. As shown in Fig. 10, while a substantial difference exists between the free-space and any hand-loaded

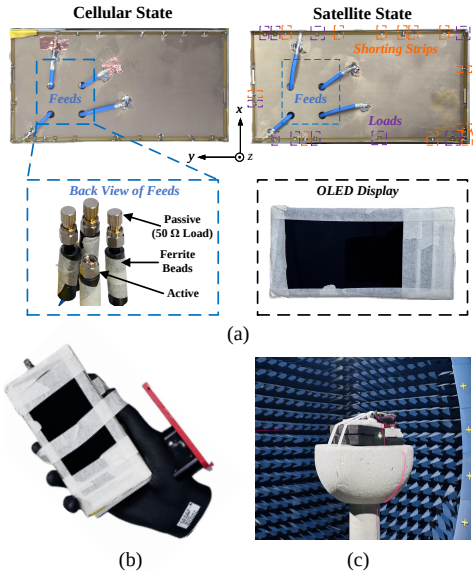

Fig. 12. (a) Fabricated prototypes of the proposed antenna systems for both cellular and satellite states. (b) The SPEAG CTIA hand phantom is used to emulate the handheld scenario. (c) Measurement setup in the Satimo anechoic chamber.

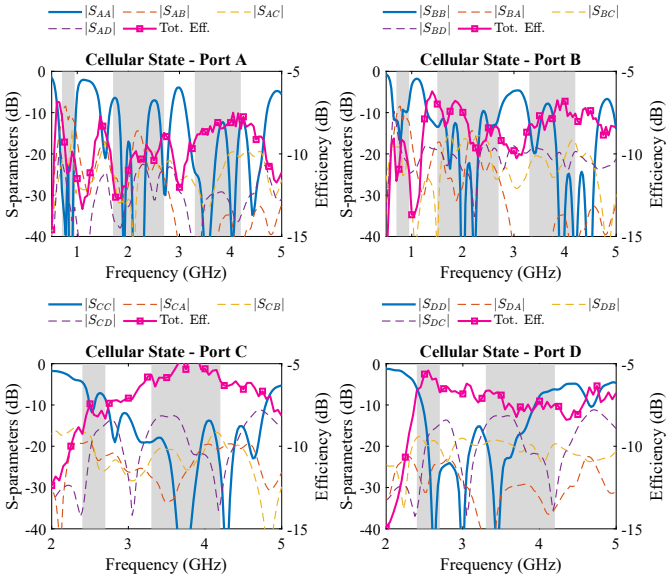

Fig. 13. Measured *S*-parameters and efficiencies of the proposed handset antennas in cellular state.

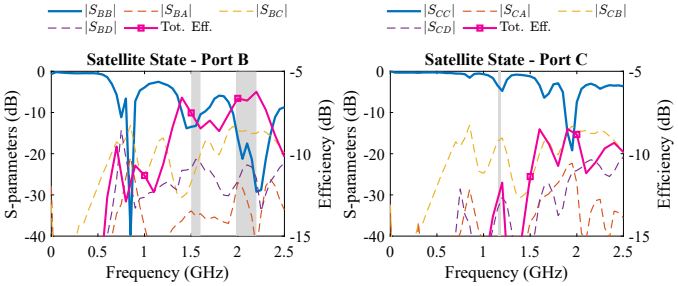

Fig. 14. Measured *S*-parameters and efficiencies of the proposed handset antennas in satellite state.

case, the intended endfire radiation in the satellite state is largely preserved across these shifted positions. This confirms that

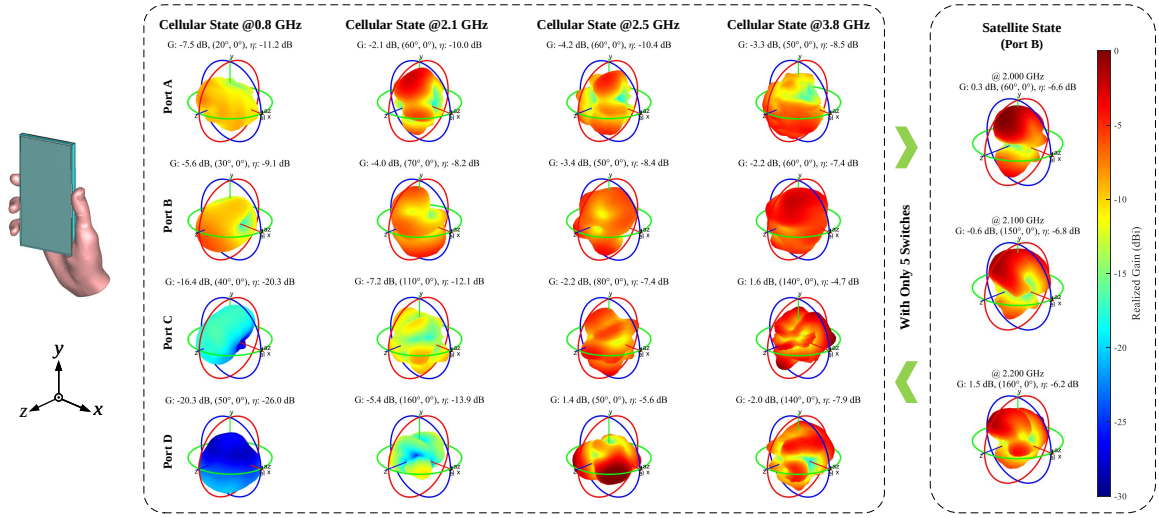

Fig. 15. Measured 3D radiation patterns of the antenna assembly under cellular and satellite operating states, with realized gains, main radiation direction, and total efficiencies annotated in each subplot. Here, G denotes the maximum realized gain, the pair (θ, φ) indicates the direction of maximum radiation, and η denotes the total efficiency.

reasonable hand position changes do not significantly degrade the SATCOM performance, since the dominant scattering environment is already established once the hand is present.

The envelope correlation coefficients (ECCs) under individual port excitations in the cellular state are calculated, which evaluates the spatial correlation between two radiation patterns by integrating their far-field components E_θ and E_φ over the elevation angle θ and the azimuth angle φ. The computed ECCs are presented in Fig. 11, which remain below 0.1, meeting the widely accepted international criterion of being less than 0.5 for MIMO systems, indicating good performance for MIMO operation.

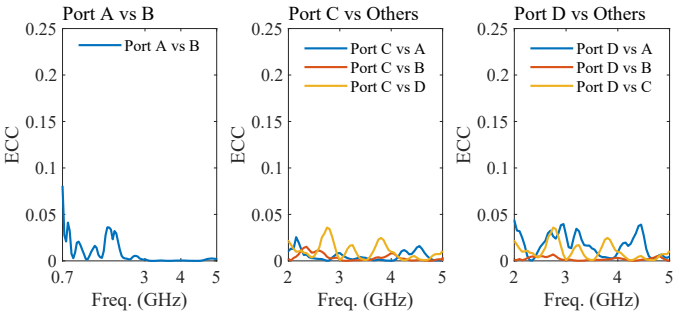

Fig. 16. Measured envelope correlation coefficients (ECCs) under individual port excitations in the cellular state.

IV. Experiment and Discussion

A. Experiment

To further validate the performance of the proposed handset antenna system, prototypes operating in both the cellular and satellite states were fabricated, with the prototypes shown in Fig. 12(a). All components and dimensions are consistent with those specified in Fig. 2. Lumped elements in 0402 packages were used and implemented using Surface-Mount Technology (SMT) technology to achieve the desired network currents. The antennas were excited through coaxial cables terminated with SMA connectors. Due to the presence of a full-screen display, four holes were drilled at the PCB of the handset, to allow the coaxial cables to exit from the back of the prototype. A SPEAG hand phantom was employed to emulate handheld user scenarios, which conformed to the CTIA standard, as depicted in Fig. 12(b). The same phantom was also integrated in full-wave simulations, ensuring consistency between simulated and experimental conditions. The following measurement results demonstrate good agreement with the simulations, thereby verifying the validity of the adopted handheld model.

The S-parameters of the fabricated prototype in both the cellular and satellite states were measured using an Agilent N5071C vector network analyzer, as shown in Fig. 13 and Fig. 14. The prototype exhibited good impedance matching within the target frequency bands, with reflection coefficients below −6 dB. The measured isolation levels were also consistent with the simulation results, exceeding 10 dB across the target frequency bands, indicating good MIMO performance.

The far-field radiation patterns of the prototypes were measured in a Satimo microwave anechoic chamber (SG24–L), with the measurement setup shown in Fig. 12(c) and the results presented in Fig. 15, following the same format as in Fig. 6. The antennas exhibited similar far-field characteristics and gain values to the simulated results within their respective frequency bands. At 2.1 GHz in the satellite state, Port B achieved distinct endfire radiation with a measured gain of -0.6 dB, representing an improvement of 3.4 dB compared to its counterpart in the cellular state. The measured efficiencies for both states are presented in Fig. 13 and Fig. 14, showing good agreement with the simulation results. Compared to the simulated results, the slight variations in gains and efficiencies could be attributed to assembly tolerances and discrepancies between the actual screen parameters and the surrogate values used in the model. The measured ECC results were shown in Fig. 16, where the values for all ports remain below 0.1 across various frequency bands. These results confirm the reliability of the proposed antenna system for satellite communication applications.

TABLE IV
COMPARISONS WITH REPRESENTATIVE HANDSET ANTENNA DESIGNS

Ref., Year	Cellular Coverage	SATCOM Coverage	Display Included?	Hand Included?	Efficiency (dB)	Method
[9], 2019	0.69–0.96 (1), 1.7–2.7 (1)	–	No	No	-1.5, -1.0	Two monopole branches + matching circuit + two ground branches
[16], 2021	3.3–5.0 (8)	–	No	No	-0.8	Dual-mode decoupling of integrated slot antenna pairs
[24], 2021	0.69–0.96 (1), 1.7–2.7 (2), 3.3–3.8 (4)	–	Yes†	Yes	-5.2(-3.2), -7.0(-1.9), -6.2(-0.8)	CMA + antenna cluster technique
[52], 2022	3.4–3.6 (4)	–	No	No	-0.46	CMA for composite PEC–lossy dielectric structures
[53], 2023	–	End-fire radiation at 2.49 GHz (CP)	No	Yes⋆	-0.70	Rectangular loop with capacitive loading and L-shaped coupled feed
[54], 2025	0.69–0.96 (1), 1.7–2.7 (1), 3.4–3.6 (1)	–	No	No	-24.0(-4.0), -2.0(-1.5), -2.8(-2.4)	Non-Foster active matching + passive branches
[55], 2025	–	End-fire radiation at 1.575 GHz (LP)	No	No	-0.4	Modified inverted-L with embedded inductor + series capacitor
[56], 2025	–	End-fire radiation at 1.9 GHz (LP)	No	No	-1.0	Capacitive-loaded tri-folded dipole in metallic frame
Proposed	0.69–0.96 (2), 1.7–2.7 (2/4) 3.3–4.2 (4)	End-fire radiation at n256 band (LP)	Yes‡	Yes	-9.7, -5.8, -6.0	Automated synthesis via internal multiport method

Note: CP denotes circular polarization, LP denotes linear polarization, CMA denotes characteristic mode analysis.
In the cellular coverage column, numbers in parentheses denote the number of antenna ports (MIMO order) per band.
In the efficiency column, the value outside parentheses reports the highest antenna-level total efficiency across the specified bands, whereas the value in parentheses reports the effective efficiency achieved with auxiliary techniques (e.g., adaptive excitation or active matching).
† Entry in which the display is modeled as a glass dielectric with an aluminum backplate. Its contribution to the overall loss is small.
‡ Entry in which the display is modeled with an ohmic-loss sheet, which yields substantially higher loss.
⋆ Entry in which a hand phantom is included and the antenna is located at the handset top and separated from the hand. Thus, the efficiency remains relatively high even under a user scenario.

To further evaluate the MIMO performance of the proposed antenna system, the frequency-dependent ergodic capacity was computed at an SNR of 20 dB using (1), where the efficiency matrix **T** was constructed from the simulated or measured total efficiencies. For each frequency point, the far-field patterns of all ports were normalized such that their solid-angle–weighted power equaled one. The spatial correlation matrix **R** was then derived from these normalized directivity patterns, and the equivalent channel matrix **H** was modeled according to (2). Monte Carlo averaging over $K = 10^4$ Rayleigh channel realizations yielded the ergodic capacity, while the Rayleigh upper bound was computed by setting both the efficiency matrix **T** and the spatial correlation matrix **R** to identity matrices, i.e., $\mathbf{T} = \mathbf{R} = \mathbf{U}$, which corresponds to the ideal case with full efficiency and completely uncorrelated ports.

Fig. 17 compares the simulated, measured, and ideal capacities. For the 2×2 configuration (0.70–0.95 GHz and 1.70–2.40 GHz), the capacity reaches approximately 5 bps/Hz. For the 4×4 configuration (2.40–2.70 GHz and 3.30–4.20 GHz), the proposed design achieves a notable capacity improvement, reaching around 11 bps/Hz, attributed to the increased spatial degrees of freedom. The close agreement between simulated and measured results further verifies the validity of the network-based modelling approach.

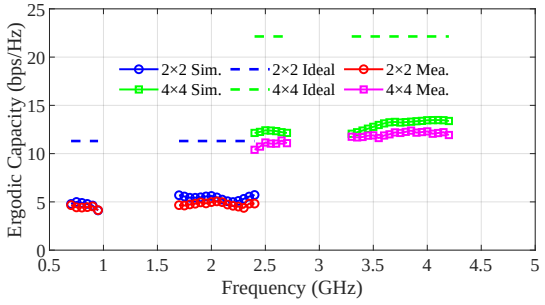

Fig. 17. Simulated and measured ergodic capacities in the cellular state under 2×2 and 4×4 configurations, along with the ideal Rayleigh reference.

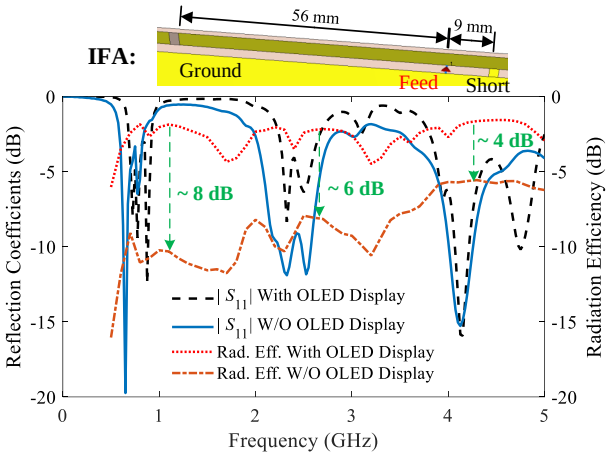

Fig. 18. Reflection coefficients and radiation efficiency of a typical inverted-F antenna (IFA) with and without an OLED display with 4.5 Ω/sq sheet resistance.

B. Discussion

Table IV summarizes representative handset multi-antenna and endfire SATCOM designs in chronological order. For consistency across heterogeneous studies, the comparison includes each design's operating bands, SATCOM capability, display integration, per-band MIMO order, and method. As indicated, the proposed design uniquely integrates an endfire SATCOM antenna into a complete cellular assembly, while requiring only five switching points for state control. In addition, the internal multiport method accounts for complex scatterers such as the

display and user proximity, thereby alleviating the design effort of frame-integrated handset antennas.

As shown in the efficiency column, the proposed antenna exhibits modest efficiencies, more pronounced in the low band. This trend is consistent with practical handset constraints, including the metallic frame and platform integration [9], absorption by lossy human tissue [57], and resistive loss in the OLED display's conductive layer [58]. In [59], an experimental study on a commercial smartphone reports total antenna efficiencies below -10 dB (10%) up to 3 GHz in free space. In [24], characteristic mode analysis is employed to design a hand-immune antenna cluster, and the reported average single-antenna efficiency in the low band remains around -8 dB ($\approx$ 15%), which is relatively higher since the OLED display's conductive sheet is not included. Including this effect typically reduces the radiation efficiency by about 4–8 dB. For illustration, Fig. 18 compares a typical IFA with and without an OLED conductive sheet with 4.5 Ω/sq sheet resistance and shows about 8 dB degradation in the low band and about 4 dB in the high band. These observations indicate that modest antenna efficiencies are common under realistic conditions. The proposed assembly is evaluated with a lossy chassis, a full-screen OLED with ultra-small clearance, and user scenarios, so modest efficiencies are expected.

Beyond platform losses, assembly-level constraints further limit efficiency. With a single feed port, the design must cover 0.69-4.2 GHz and maintain inter-antenna isolation. These requirements reduce the effective degrees of freedom available to each band and introduce a trade-off between bandwidth and efficiency. Under the Cellular state, Ports A and B are therefore constrained, and their efficiencies are modest. This trend is reflected in Fig. 5, which shows only small efficiency improvements at Ports A and B relative to the reference, which uses the same feed position but no added loading or shorting strips for current regulation. By contrast, Ports C and D operate over narrower ranges of 2.4–2.7 GHz and 3.3–4.2 GHz and achieve larger improvements of 2–3 dB. Because the design integrates all required antennas within a limited handset volume, the peak efficiency for any single band is generally lower than for a design dedicated to one or two bands.

Regarding practical considerations, the present study is demonstrated on a metal-frame-integrated handset architecture. Extension to planar, printed handset antennas would require additional engineering adaptation. Moreover, the biasing network of the PIN diodes introduces parasitic effects that may affect efficiency and isolation. A complete system-level co-design with the RF front-end and device hardware lies beyond the antenna-level scope of this work but represents an important aspect for future integration. The optimization code and the associated multiport dataset are made publicly available in a repository for academic use [60].

V. Conclusion

In this paper, a network-based method is proposed for realizing a reconfigurable handset antenna assembly that operates efficiently in both cellular and satellite states. By integrating internal port modeling with an automated topology synthesis framework, the design enables intelligent placement of feeds and reactive loads with minimal manual intervention. The resulting antenna configuration achieves reliable impedance matching, high isolation, and wide-beam endfire radiation across multiple frequency bands. A compact implementation using only five switchable elements enables seamless state transition with low hardware complexity, supporting turnkey integration into modern smartphone platforms. Full-wave simulations and prototype measurements validate the performance under realistic usage conditions, demonstrating the practicality of the proposed design for compact, multifunctional terminal applications.

References

[1] J. Anguera, A. Andújar, M.-C. Huynh, C. Orlenius, C. Picher, and C. Puente, "Advances in antenna technology for wireless hand-held devices," *Int. J. Antennas Propag.*, vol. 2013, Nov. 2013, Art. no. 838364.

[2] W. Hong, "Solving the 5G mobile antenna puzzle: Assessing future directions for the 5G mobile antenna paradigm shift," *IEEE Microw. Mag.*, vol. 18, no. 7, pp. 86–102, Nov.–Dec. 2017.

[3] H. Zhang, Z. Wang, J. Yu, and J. Huang, "A compact MIMO antenna for wireless communication," *IEEE Antennas Propag. Mag.*, vol. 50, no. 6, pp. 104–107, Dec. 2008.

[4] Z. Zhang, *Antenna Design for Mobile Devices*, 2nd ed. Hoboken, NJ, USA: Wiley, 2017.

[5] D. Wu, S. W. Cheung, and T. I. Yuk, "A compact and low-profile loop antenna with multiband operation for ultra-thin smartphones," *IEEE Trans. Antennas Propag.*, vol. 63, no. 6, pp. 2745–2750, Jun. 2015.

[6] A. Zhao and Z. Ren, "Size reduction of self-isolated MIMO antenna system for 5G mobile phone applications," *IEEE Antennas Wireless Propag. Lett.*, vol. 18, no. 1, pp. 152–156, Jan. 2019.

[7] A. Ren, Y. Liu, and C.-Y.-D. Sim, "A compact building block with two shared-aperture antennas for eight-antenna MIMO array in metal-rimmed smartphone," *IEEE Trans. Antennas Propag.*, vol. 67, no. 10, pp. 6430–6448, Oct. 2019.

[8] Y. Ye, X. Zhao, and J. Wang, "Compact high-isolated MIMO antenna module with chip capacitive decoupler for 5G mobile terminals," *IEEE Antennas Wireless Propag. Lett.*, vol. 21, no. 5, pp. 928–932, May 2022.

[9] D. Huang, Z. Du, and Y. Wang, "Eight-band antenna for full-screen metal frame LTE mobile phones," *IEEE Trans. Antennas Propag.*, vol. 67, no. 3, pp. 1527–1534, Mar. 2019.

[10] H.-D. Chen, Y.-C. Tsai, C.-Y.-D. Sim, and C. Kuo, "Broadband eight-antenna array design for sub-6 GHz 5G NR bands metal-frame smartphone applications," *IEEE Antennas Wireless Propag. Lett.*, vol. 19, no. 7, pp. 1078–1082, Jul. 2020.

[11] X.-T. Yuan, Z. Chen, T. Gu, and T. Yuan, "A wideband PIFA-pair-based MIMO antenna for 5G smartphones," *IEEE Antennas Wireless Propag. Lett.*, vol. 20, no. 3, pp. 371–375, Mar. 2021.

[12] M. F. Khajeim, G. Moradi, R. S. Shirazi, and S. Zhang, "Broadband dual-polarized antenna array with endfire radiation for 5G mobile phone applications," *IEEE Antennas Wireless Propag. Lett.*, vol. 20, no. 12, pp. 2427–2431, Dec. 2021.

[13] A. Ren, H. Yu, L. Yang, Z. Huang, Z. Zhang, and Y. Liu, "A broadband MIMO antenna based on multimodes for 5G smartphone applications," *IEEE Antennas Wireless Propag. Lett.*, vol. 22, no. 7, pp. 1642–1646, Jul. 2023.

[14] L. Sun, Y. Li, Z. Zhang, and H. Wang, "Self-decoupled MIMO antenna pair with shared radiator for 5G smartphones," *IEEE Trans. Antennas Propag.*, vol. 68, no. 5, pp. 3423–3432, May 2020.

[15] L. Sun, Y. Li, Z. Zhang, and Z. Feng, "Wideband 5G MIMO antenna with integrated orthogonal-mode dual-antenna pairs for metal-rimmed smartphones," *IEEE Trans. Antennas Propag.*, vol. 68, no. 4, pp. 2494–2503, Apr. 2020.

[16] L. Sun, Y. Li, and Z. Zhang, "Wideband decoupling of integrated slot antenna pairs for 5G smartphones," *IEEE Trans. Antennas Propag.*, vol. 69, no. 4, pp. 2386–2391, Apr. 2021.

[17] W. Hu, X. Zhang, Y. Cui, H. Wang, and Y. Cheng, "Dual-band antenna pair with high isolation using multiple orthogonal modes for 5G smartphones," *IEEE Trans. Antennas Propag.*, vol. 71, no. 2, pp. 1949–1954, Feb. 2023.

[18] L. Cui, J. Guo, Y. Liu, and C.-Y.-D. Sim, "An 8-element dual-band MIMO antenna with decoupling stub for 5G smartphone applications," *IEEE Antennas Wireless Propag. Lett.*, vol. 18, no. 10, pp. 2095–2099, Oct. 2019.

[19] J.-N. Hwang and F.-C. Chen, "Reduction of the peak SAR in the human head with metamaterials," *IEEE Trans. Antennas Propag.*, vol. 54, no. 12, pp. 3763–3770, Dec. 2006.
[20] Y. G. Kim and W. Hong, "Radiation efficiency-improvement using a vialess, planar ZOR antenna for wireless ECG sensors on a lossy medium," *IEEE Antennas Wireless Propag. Lett.*, vol. 13, pp. 1211–1214, 2014.
[21] M. Berg and E. Salonen, "Compensating for the influence of human hand with two switchable antennas," *IET Microw., Antennas Propag.*, vol. 5, no. 13, pp. 1576–1582, 2011.
[22] S. Zhang, K. Zhao, Z. Ying, and S. He, "Adaptive quad-element multi-wideband antenna array for user-effective LTE MIMO mobile terminals," *IEEE Trans. Antennas Propag.*, vol. 61, no. 8, pp. 4275–4283, Aug. 2013.
[23] P. Ylä-Oijala, A. Lehtovuori, and R. Luomaniemi, "Characteristic mode analysis of mobile and wearable antennas in lossy environment," in *Proc. 2020 14th Eur. Conf. Antennas Propag. (EuCAP)*, 2020, pp. 1–5.
[24] R. Luomaniemi, P. Ylä-Oijala, A. Lehtovuori and V. Viikari, "Designing hand-immune handset antennas with adaptive excitation and characteristic modes," *IEEE Trans. Antennas Propag.*, vol. 69, no. 7, pp. 3829–3839, Jul. 2021.
[25] Y. Luo, L. Zhu, Y. Liu, Y. Xu, N. Liu, and S. Gong, "Efficiency improvement of smartphone antennas using higher-order mode suppression under characteristic mode analysis," *IEEE Trans. Antennas Propag.*, vol. 70, no. 11, pp. 10304–10317, Nov. 2022.
[26] H. Li, W. Zheng, Y. Diao, and Q. Wu, "Alleviating user interaction for handset antennas with reactive loads," *IEEE Trans. Antennas Propag.*, vol. 72, no. 7, pp. 6069–6074, Jul. 2024.
[27] M. Y. Liang, X. Y. Li, X. T. Tian, H. B. Zhang, and H. H. Zhang, "Satellite communication smartphone circularly polarized antenna," in *Proc. 2024 14th Int. Symp. Antennas, Propag. EM Theory (ISAPE), Hefei, China*, 2024, pp. 1–2.
[28] X. Zhang, K. Wei, Y. Li, and Z. Zhang, "A polarization reconfigurable antenna for satellite communication in foldable smartphone," *IEEE Trans. Antennas Propag.*, vol. 71, no. 12, pp. 9938–9943, Dec. 2023.
[29] S. Rao and Y. Wang, "Design of octa-band mobile antenna in metal-bezel smartphone with wide beamwidth in the endfire direction for n256-band satellite communications," *IEEE Trans. Antennas Propag.*, vol. 72, no. 9, pp. 7335–7340, Sept. 2024.
[30] S. Rao and Y. Wang, "Shared-aperture design of the cellular antenna and satellite communication antenna with circular polarization in S-band for metal-bezel smartphones," *IEEE Trans. Antennas Propag.*, vol. 72, no. 5, pp. 3938–3949, May 2024.
[31] X. Zhang, K. Wei, Y. Li, and Z. Zhang, "A circularly polarized antenna based on narrowed crossed dipole for smartphone satellite communication," *IEEE Antennas Wireless Propag. Lett.*, vol. 23, no. 8, pp. 2511–2515, Aug. 2024.
[32] Y. Meng et al., "Metasurface-loaded circularly polarized dual-band MIMO cellphone frame antenna for mobile communication applications," *IEEE Antennas Wireless Propag. Lett.*, 2025.
[33] M. Wang, L. Chang, Q. Li, and A. Zhang, "Modified inverted-L antenna with improved upper hemisphere ratio and ground-independent performance for augmented mobile satellite service," *IEEE Trans. Antennas Propag.*, 2024.
[34] S. Soltani, P. Lotfi, and R. D. Murch, "Design and optimization of multiport pixel antennas," *IEEE Trans. Antennas Propag.*, vol. 66, no. 4, pp. 2049–2054, Apr. 2018.
[35] S. Shen, C.-Y. Chiu, and R. D. Murch, "Multiport pixel rectenna for ambient RF energy harvesting," *IEEE Trans. Antennas Propag.*, vol. 66, no. 2, pp. 644–656, Feb. 2018.
[36] F. Jiang, C.-Y. Chiu, S. Shen, Q. S. Cheng, and R. Murch, "Pixel antenna optimization using N-Port characteristic mode analysis," *IEEE Trans. Antennas Propag.*, vol. 68, no. 5, pp. 3336–3347, May 2020.
[37] W. Zheng, H. Li, and G. Liu, "Design of circularly polarized smartwatch antenna with reactive loads," *IEEE Antennas Wirel. Propag. Lett.*, vol. 22, no. 7, pp. 1602–1606, Jul. 2023.
[38] W. Zheng, Y. Yang, and H. Li, "Design of polarization reconfigurable pixel antennas with optimized PIN-diode implementation," *IEEE Trans. Antennas Propag.*, vol. 73, no. 2, pp. 851-862, Feb. 2025.
[39] C. Zhang, S. Liao, and M. Li, "Scattering matrix based IMPM for multiport antenna systems," *IEEE Antennas Wireless Propag. Lett.*, online.
[40] A. Goldsmith, "Wireless communications," *Cambridge Univ. Press*, Cambridge, U.K., 2005.
[41] R. Y. Tian, B. K. Lau, and Z. Ying, "Multiplexing efficiency of MIMO antennas," *IEEE Antennas Wireless Propag. Lett.*, vol. 10, pp. 183–186, 2011.
[42] D. Tse and P. Viswanath, *Fundamentals of Wireless Communication*, Cambridge University Press, 2005.
[43] K. Deb and H. Jain, "An evolutionary many-objective optimization algorithm using reference-point-based nondominated sorting approach, part I: solving problems with box constraints," *IEEE Trans. Evol. Comput.*, vol. 18, no. 4, pp. 577–601, 2013.
[44] C. Han, D. Chen, Y. Gong, Z. Zhang, Y. Wang and L. Wang, "An improved NSGA-III based unmanned airborne conformal array beam pattern optimization," in *2022 IEEE 5th International Conference on Electronic Information and Communication Technology (ICEICT)*, Hefei, China, 2022, pp. 661–664.
[45] A. Nysaeter, "Two-way MIMO sparse array antenna optimization with NSGA-III," in *2020 IEEE Radar Conference (RadarConf20)*, Florence, Italy, 2020, pp. 1–6.
[46] W. Zheng, Y. Yang, T.-X. Feng and H. Li, "Systematic inverse design of miniaturized frequency selective surfaces based on microwave network theory and NSGA-III," *IEEE Trans. Microw. Theory Techn.*, online.
[47] R. Rodríguez-Cano, *Test Plan for Wireless Device Over-the-Air Performance*, CTIA Certification Program, Washington, DC, USA, 2014.
[48] H. Gao, X. Chen, Y. Liu, and G. F. Pedersen, "Antenna performance over-the-air testing of 5G commercial smartphones," *IEEE Trans. Instrum. Meas.*, vol. 73, pp. 1–8, Mar. 2024.
[49] *CST Microwave Studio*, CST Studio Suite, Dearborn, MI, USA, 2025.
[50] MathWorks, Inc., *MATLAB and Simulink for Technical Computing*, Version R2024a, Natick, MA, USA, 2024.
[51] 3GPP, *NR; User Equipment (UE) radio transmission and reception; Part 1: Range 1 Standalone (Release 17)*, 3rd Generation Partnership Project (3GPP), TS 38.101-1 V17.10.0, 2023.
[52] H. Zhang, X.-Z. Liu, G.-S. Cheng, Y. Liu, G.-G. Yu, and G.-M. Shi, "Low-SAR four-antenna MIMO array for 5G mobile phones based on the theory of characteristic modes of composite PEC–lossy dielectric structures," *IEEE Trans. Antennas Propag.*, vol. 70, no. 3, pp. 1623-1631, Mar. 2022.
[53] Z. Cao, L. Chang, Y. Li, K. Wei, and Z. Zhang, "Compact mobile terminal antenna with endfire circularly polarized beam for satellite communications," *IEEE Trans. Antennas Propag.*, vol. 71, no. 12, pp. 9980–9985, Dec. 2023.
[54] D. Li, C. Deng, and Y. Zhang, "Miniaturized multi-band smartphone antenna using Non-Foster-based active matching below 1 GHz," *IEEE Trans. Antennas Propag.*, early access, 2025.
[55] M. Wang, L. Chang, Q. Li, and A. Zhang, "Modified inverted-L antenna with improved upper hemisphere ratio and ground-independent performance for augmented mobile satellite service," *IEEE Trans. Antennas Propag.*, early access, 2025.
[56] P. Li, M. Hu, Y. Zhang, P. Liang, Y. Li, and Z. Zhang, "Wide-beam metallic bezel antenna for direct satellite-to-handset communications," *IEEE Trans. Antennas Propag.*, early access, 2025.
[57] R. Khan, A. A. Al-Hadi, and P. J. Soh, "Recent advancements in user effect mitigation for mobile terminal antennas: a review," *IEEE Trans. Electromagn. Compat.*, vol. 61, no. 1, pp. 279–287, Feb. 2019.
[58] Z. J. Silva, C. R. Valenta, and G. D. Durgin, "Optically transparent antennas: a survey of transparent microwave conductor performance and applications," *IEEE Antennas Propag. Mag.*, vol. 63, no. 1, pp. 27–39, Feb. 2021.
[59] L. A. Bronckers, A. Roc'h, and A. B. Smolders, "Benchmarking a high-end smartphone's antenna efficiencies," *IEEE Access*, vol. 7, pp. 105680–105686, 2019.
[60] W. Zheng, "Turnkey-Handset-Antenna," 2025. [Online]. Available: https://github.com/wenruizheng/Turnkey-Handset-Antenna

Wenrui Zheng (Graduate Student Member, IEEE) was born in Wuxi, China, in 1999. He received the B.S. degree (Hons.) in communication engineering from Dalian Maritime University, Dalian, China, in 2022. He is currently pursuing the Ph.D. degree with Dalian University of Technology, Dalian.

His current research interests include characteristic mode (CM) analysis, terminal antennas, pixel antennas, and electromagnetic metamaterials. Mr. Zheng was a recipient of the IEEE APS Eugene F. Knott Pre-Doctoral Research Grant in 2023. He is serving as a reviewer for *IEEE Antennas and Wireless Propagation Letters*.

Yunlai Yang was born in Xuchang, China, in 2001. He received the B.S. degree in electronic information science and technology from Dalian Maritime University, Dalian, China, in 2023. He is currently pursuing the Ph.D. degree with Dalian University of Technology, Dalian.

His current research interests include pixel antennas and reflectarray antennas.

Yan Wang (Senior Member, IEEE) received the B.S. degree (Hons.) in electronic information science and technology from the University of Electronic Science and Technology of China, Chengdu, China, in 2011, and the Ph.D. degree in electronic engineering from Tsinghua University, Beijing, China, in 2016.

In September 2016, he joined Huawei Technology Ltd., Shanghai, China, as a Senior Antenna Engineer. In January 2020, he joined VIVO Shanghai Research Center, Shanghai, as an Antenna Director and Antenna Expert. Since February 2021, he has been with Fudan University, Shanghai, where he is currently a Tenured-Track Associate Professor. His current research interests include antenna theory and design, especially the antenna technology for mobile devices, base stations, and radar.

Dr. Wang is serving as an Associate Editor for the *IET Electronic Letters* and the Youth Editorial Board Member for the *Journal of Microwaves* (in Chinese). He is also serving as a reviewer for *IEEE Transactions on Antennas and Propagation* and *IEEE Antennas and Wireless Propagation Letters*.

Can Ding (Senior Member, IEEE) received the bachelor's degree in integrated circuit and integrated system from Xidian University, Xi'an, China, in 2009, and the joint Ph.D. degree in electromagnetic fields and microwave technology from Xidian University and Macquarie University, Sydney, NSW, Australia, in 2016.

From 2015 to 2017, he was a Post-Doctoral Research Fellow with the University of Technology Sydney (UTS), Ultimo, NSW, Australia, where he is currently an Associate Professor with the Faculty of Engineering and IT (FEIT) and a Core Member of the Global Big Data Technologies Center (GBDTC). His accomplishments encompass several research and industry projects, patented innovations, and a portfolio of over 120 publications in top-tier journals and conferences.

He was an ARC DECRA Fellow from 2020 to 2024. Since 2024, he has served as an Associate Editor for *IEEE Antennas and Wireless Propagation Letters* (AWPL). He was recognized as a Top Reviewer for *IEEE Transactions on Antennas and Propagation* (TAP) for four consecutive years (2022–2025). He also received the distinction of Outstanding Reviewer for *IEEE AWPL* for three consecutive years (2023–2025) and was named an Outstanding Associate Editor in 2025. Since late 2023, he has been a member of the IEEE AP-S Education Committee and the EurAAP Working Group on Early Careers, and since 2025 he has also served on the IEEE AP-S Technical Committee 4 on Metamaterials. He was selected as a 2024 IEEE AP-S Young Professional Ambassador and has served on the IEEE AP-S Young Professional Committee since 2025.

Hui Li (Senior Member, IEEE) received the Ph.D. degree in electrical engineering from the Royal Institute of Technology (KTH), Stockholm, Sweden, in 2012.

From 2012 to 2015, she was a Post-Doctoral Researcher at the Department of Electrical and Information Technology, Lund University, Lund, Sweden. Since 2015, she has been with Dalian University of Technology, Dalian, China, where she is currently a Professor. Her current research interests include terminal antennas, wearable antennas, theory of characteristic mode (CM), RFID antennas, antenna–user interactions, millimeter-wave antennas, and microwave imaging.

Dr. Li is a member of the Education Committee of the IEEE Antennas and Propagation Society (AP-S), where she has served as the final Judge for the IEEE AP-S Student Design Contest. She was elected as the 2023 IEEE APS Young Professional Ambassador. She received the CST University Publication Award in 2013 and the IEEE Women in NEMO for MAPE Award in 2020. She is an Associate Editor of *IEEE Antennas and Wireless Propagation Letters*.